

Dye degradation using piperazine encapsulated biosynthesized iron nanoparticles

Sathiya Selvaraj^{1*}, Durairaj Sankaran², Ilangkumaran Mani³

^{1*}Department of Chemistry, Selvam College of Technology, Namakkal, Tamil Nadu, India

²Department of Electrical & Electronics Engineering, Annapoorna Engineering College, Salem, Tamil Nadu, India

³Department of Mechanical Engineering, Knowledge Institute of Technology, Salem, Tamil Nadu, India

Received 4.9.2024.

Revised 18.4.2025.

Accepted 16.5.2025.

<https://doi.org/10.2298/CICEQ240904010S>

Abstract

This study investigates the breakdown of aniline yellow dye using biosynthesized iron nanoparticles that uses extract from *Eryngium billardieri*. Piperazine encapsulation in a chlorinated environment increased degradation efficiency, reaching up to 92% in the dark and 96% under photocatalytic conditions. Ultraviolet-visible spectroscopy (331.24 nm, 243.19 nm), Fourier Transform Infrared Spectroscopy (Fe–O at 539 cm⁻¹, C–N at 1231 cm⁻¹), X-ray Diffraction analysis (peaks at 26.31° to 76.84°, indicating FCC structure), and Energy Dispersive Spectroscopy (Fe and Cl presence) were used to characterize the nanoparticles. The N-functionalities produced from piperazine and Fe²⁺ (712 eV) were validated by X-ray Photoelectron Spectroscopy. Spherical, evenly distributed particles (10–30 nm) with core-shell morphology were seen by Field Emission Scanning Electron Microscopy and High Resolution Transmission Electron Microscopy. After encapsulation, Photoluminescence analysis showed less electron-hole recombination. Mesoporosity (type IV isotherms) was revealed by Brunauer-Emmett-Teller analysis, and the piperazine coating reduced surface area. Superparamagnetic behaviour with a blocking temperature close to 35K was found via magnetic measurements. High stability, catalytic efficiency, and potential for environmental remediation were all displayed by the encapsulated iron nanoparticles.

Keywords: dye degradation, *Eryngium billardieri*, iron nanoparticles, photocatalysis, piperazine.

Introduction

The textile industry is one of the largest sectors in the global economy, but it is also one of the most polluting, thanks to the widespread use of synthetic dyes. These dyes, with their complex aromatic structures, are highly resistant to degradation and pose significant environmental and health risks if released untreated into natural water bodies. The improper disposal of textile wastewater has resulted in severe contamination of aquatic ecosystems, threatening both marine life and human health [1]. The toxicity of textile waste, particularly when dumped in the environment without proper treatment, has been well documented. According to studies, chemicals in textile effluents, including dyes, are toxic, carcinogenic, and mutagenic, posing serious health risks to humans and animals [2]. Furthermore, the presence of these dyes in water bodies causes reduced light penetration, disrupting photosynthesis and affecting aquatic ecosystems [3]. The impact of textile waste on aquatic systems is significant. The dyes can form a layer on the surface of water bodies, preventing sunlight from penetrating and sustaining aquatic life. This disruption may cause a decrease in the oxygen levels in the water, resulting in the death of fish and other marine organisms [4]. Furthermore, the accumulation of dyes in sediments can cause long-term ecological damage, affecting biodiversity in the affected areas [5]. Traditional methods for degrading textile dyes, such as physical and chemical treatments, are limited in terms of efficiency, cost, and environmental impact. Biological methods, while environmentally friendly, frequently lack the required speed and efficacy [6]. Recent advances in nanotechnology have opened up new possibilities for the degradation of these persistent pollutants. Biosynthesized nanoparticles, in particular, have shown great promise due to their unique properties and environmentally friendly synthesis processes [7]. Advanced oxidation processes, such as photocatalysis, Fenton reactions, and ozonation, have emerged as efficient dye degradation methods. These techniques depend on the production of reactive oxygen species to break down complex dye molecules into simpler, less harmful compounds [8]. The combination of nanotechnology and advanced oxidation processes has further improved degradation efficiency, providing a synergistic approach to pollutant removal [9]. Nanoparticles, with their high surface area-to-volume ratio and unique electronic properties, have been extensively studied for their catalytic abilities in dye degradation. Biosynthesized nanoparticles, in particular, are gaining attention for their green synthesis methods, which avoid the use of hazardous chemicals [10]. These nanoparticles can efficiently catalyze the breakdown of dye molecules, making them a promising tool in wastewater treatment [11]. Nanoparticles can be synthesized using a variety of methods, including physical, chemical, and biological routes. Biological synthesis, also known as biosynthesis, is the environmentally friendly process of producing nanoparticles using microorganisms, plants, or other biological materials. This method not only reduces the use of toxic chemicals, but also improves the biocompatibility and functionality of

nanoparticles [12]. Different synthesis methods can be optimized to improve nanoparticles' performance in degrading textile dyes [13]. Coating and immobilization techniques can significantly improve the efficacy of nanoparticles for dye degradation. Coating nanoparticles with specific materials can enhance their stability, dispersibility, and reusability, making them more effective in catalytic processes [14]. Immobilization on solid supports can prevent nanoparticle aggregation, facilitate their recovery and reuse, and thus reduce the operational costs and environmental impact of the treatment process [15]. The degradation of textile dyes using biosynthesized nanoparticles is a promising and long-term solution to the environmental problems caused by textile wastewater.

Green nanotechnology has seen significant growth in recent years because of its eco-friendly methodology and potential uses in environmental restoration. A new method for boosting photocatalytic, antibacterial, and antioxidant properties is the creation of metal and metal oxide nanoparticles utilising plant extracts in conjunction with doping techniques. Highlighting the potential of phytochemical routes in boosting catalytic behaviour, Kumar et al. (2024) examined the photocatalytic and antioxidant performance of Co/Ni-doped haematite nanoparticles synthesized using chemical and green approaches [16]. The importance of medicinal plants in nanoparticle synthesis was further supported by Sharma et al. (2025), who used *Vitex negundo* leaf extract to create Ni and Nd-doped ZnO nanoparticles and reported notable photocatalytic and antibacterial activities [17].

Using polymer and phytochemical mediation, Kumar et al. (2025) showed how to synthesise Cu/Zn-doped haematite nanoparticles in an environmentally benign manner while demonstrating exceptional photocatalytic effectiveness and biological compatibility [18]. Using *Murraya Koenigii* extract, Verma et al. (2025) created (Fe, Al)-doped ZnO nanoparticles using a microwave-assisted green technique, achieving significant photocatalytic destruction of contaminants as well as noteworthy antibacterial and antioxidant properties [19]. Similar multifunctional activity was observed by Devi et al. (2024) in Zn and Gd-doped manganese oxide nanoparticles made with *Pinus roxburghii*, highlighting their potential for antifungal and antibacterial uses [20]. The effectiveness of Co/Zn-doped α -Fe₂O₃ nanoparticles in water filtration was further highlighted by Kumar et al. (2024), demonstrating their superior efficiency and biological safety [21].

Thakur et al. [22] investigated the production of chromium and yttrium-doped cobalt oxide nanoparticles with improved multifunctional performance using a green technique. Similarly, Rana et al. [23] studied zinc oxide and yttrium-doped zinc oxide nanoparticles, emphasizing their potential for photocatalytic degradation and biological applications. Iron oxide nanoparticles have also attracted substantial interest, with Kumar et al. [24] evaluating their origins, advances, and future possibilities in catalysis and

environmental remediation. Furthermore, Kumar et al. [25] emphasized the importance of nano-bioaugmentation in textile dye cleanup, providing a long-term strategy to health and environmental management.

Thakur and Thakur [26] synthesised Co-Ni-doped TiO₂ nanocatalysts having a spherical anatase phase, which efficiently degraded textile colors and scavenged them. Kumar et al. [27] used *Azadirachta indica* leaf extract to study the stability, reusability, and efficacy of trimetallic doped haematite (α -Fe₂O₃) nanoparticles for photocatalytic dye removal. Kumar et al. [28] investigated Ni-Zn-doped haematite nanoparticles synthesised from Polyvinylpyrrolidone and *Azadirachta indica* leaf extract, which showed improved photocatalytic and radical scavenging characteristics. Thakur and Kumar [29] investigated the effect of shape and size on Co/Ni/Zn triple-doped α -Fe₂O₃ nanoparticles, exhibiting enhanced photocatalytic and antioxidant properties.

Aquatic ecosystems and human health are seriously threatened by the rising concentrations of synthetic dyes in wastewater, especially from the textile and pharmaceutical sectors. There is a pressing need for more sustainable and effective remediation technologies because conventional treatment procedures frequently fail to remove these persistent contaminants. By combining plant-mediated synthesis and nanomaterial doping to improve photocatalytic and antibacterial capabilities, recent developments in green nanotechnology provide encouraging answers. Nevertheless, there are still issues with scalability, environmental compatibility, and attaining high efficiency in both light and dark environments.

Green-synthesised doped metal oxide nanoparticles for environmental applications have been the subject of numerous investigations. Verma et al. (2024) showed improved antioxidant and antibacterial qualities in (Cu, Ce) dual-doped ZnO nanoparticles made utilising *Colocasia esculenta* in a microwave-assisted green method [30]. Similarly, Co/Ni/Zn triple-doped α -Fe₂O₃ nanoparticles' size and shape greatly affected their photocatalytic and radical scavenging capabilities, according to Thakur and Kumar (2024), highlighting the significance of carefully planned nanostructure design [31]. The efficiency of green ZnO nanoparticles in breaking down methyl orange dye was highlighted by Thakur et al. (2022), however they also acknowledged that degradation rates varied depending on the environment [32].

The creation of linked doped TiO₂ nanoparticles, which have demonstrated exceptional photocatalytic, adsorption, and scavenging properties, is another invention (Thakur & Thakur, 2024) [33]. Furthermore, demonstrating the transdisciplinary potential of phytonanotechnology, Balkrishna et al. (2023) highlighted the use of medicinal plant extracts such as *Catharanthus roseus* and *Ocimum tenuiflorum* in the synthesis of biocompatible silver nanoparticles for disease management [34].

By investigating the synthesis, characterization, and application of these nanoparticles, this study hopes to contribute to the development of efficient and environmentally friendly wastewater treatment technologies. The combination of nanotechnology and advanced degradation methods demonstrates the potential for significant advances in environmental remediation.

This research stands out for employing *Eryngium billardieri* extract in the green synthesis of iron nanoparticles, followed by encapsulation with piperazine to enhance their structural and functional properties. The combined approach would significantly boost nanoparticle stability, dispersion, and catalytic activity. By improving both photocatalytic and magnetic properties, this method enables more efficient degradation of aniline yellow dye under both dark and light-driven conditions. The innovative piperazine coating is intended to effectively minimize particle agglomeration, promote uniform size distribution, and enhance superparamagnetic behavior.

Despite many research investigations on green-synthesized nanoparticles utilizing plant extracts, little attention has been paid to the use of *Eryngium billardieri* for the biosynthesis of iron nanoparticles, particularly when combined with piperazine encapsulation. While previous research has investigated various doped and plant-mediated nanomaterials for photocatalytic and biomedical applications, there is still a significant gap in developing multifunctional iron-based nanomaterials that combine enhanced photocatalytic efficiency, magnetic responsiveness, and environmental stability using eco-friendly methods. Furthermore, few research have examined their efficacy in degrading persistent industrial colors such as aniline yellow in both dark and light situations. This study fills a gap by introducing a novel, dual-functional approach—biosynthesizing iron nanoparticles using *Eryngium billardieri* extract and encapsulating them with piperazine.

Materials & Methods

In this investigation, Iron nanoparticles were synthesized utilizing a green method that used *Eryngium billardieri* plant extract as a reducing and stabilizing agent. To improve stability and minimize agglomeration, the synthesized iron nanoparticles were encapsulated in piperazine. This dual-functional synthesis approach intended to improve the nanoparticles' dispersibility. The resultant piperazine-encapsulated iron nanoparticles were characterized and tested for photocatalytic effectiveness in degrading organic dyes under both dark and photocatalytic environment.

Chemicals and extract preparation

The chemicals used in this study included ferrous sulphate heptahydrate, sodium borohydroxide, sodium hydroxide, 3-chloropropyl-trimethoxysilane, aniline yellow dye, hydrochloric acid, piperazine, and

deionised water. Hydrochloric acid was used to clean and dry beakers, funnels, and other chemical processing equipment before use. *Eryngium billardieri* bioextract was freshly prepared by collecting the plant material and thoroughly washing it with distilled water to remove dirt and impurities. Information regarding the grade, purity and company for each chemical used has been added in Table 1.

.Table 1. Details of chemicals used in the experiments

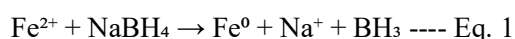
Chemical Name	Grade	Purity (%)	Supplier/Company
Ferrous Sulphate Heptahydrate (FeSO ₄ ·7H ₂ O)	Analytical	99	Merck, India
Sodium Borohydride (NaBH ₄)	Analytical	98	Sigma-Aldrich, India
Sodium Hydroxide (NaOH)	Analytical	98	Agsar Chemicals, India
Dichloromethane (CH ₂ Cl ₂)	Laboratory	99	Agsar Chemicals, India
3-Chloropropyl-trimethoxysilane (CPTS)	Laboratory	97	Sigma-Aldrich, USA
Potassium bromide (KBr)	Laboratory	98	Agsar Chemicals, India
Hydrochloric Acid (HCl)	Analytical	37 (Conc.)	Merck, India
Aniline Yellow Dye	Laboratory	98	SD Fine Chem, India
Piperazine	Laboratory	99	Sigma-Aldrich, USA
Deionised Water	Laboratory	-	In-house Preparation
<i>Eryngium billardieri</i> bioextract	-	-	Freshly Prepared (In-house)

The plant material was cleaned and air-dried at room temperature until completely moisture-free. After drying, the plant material was finely ground into powder with a mechanical grinder. This powder was combined with a suitable solvent, usually ethanol or methanol, and continuously stirred for 24 hours to extract the bioactive compounds. The mixture was then filtered to remove any solid residues, yielding a fresh bioextract ready for use in experiments [35].

Fe nanoparticles synthesis and piperazine encapsulation

The filtered *Eryngium billardieri* extract was centrifuged for 20 minutes before passing through a Millipore filter. A 0.01M solution of Ferrous sulphate heptahydrate was prepared, and the *Eryngium billardieri* extract was combined with this solution in a 4:1 ratio using a magnetic stirrer at room

temperature. The bio-synthesized iron nanoparticles were washed three times with deionised water and ethanol before drying in a flask oven at 80 degrees Celsius. For chemically synthesized iron nanoparticles, 1.3336 g of ferrous sulphate heptahydrate was mixed with 2.208 g of sodium borohydride in 160 ml of deionised water and stirred until completely dissolved. The pH was maintained at 6, the solution was cooled to near-freezing, and the mixture was vigorously stirred at 1500 rpm. The synthesis took place at room temperature. The iron nanoparticles were then separated by centrifugation at 6000 rpm for 15 minutes using neodymium magnets, followed by filtering and drying in a vacuum for 10 hours. To prevent contamination, the iron nanoparticles synthesized by *Eryngium billardieri* were stored at ambient temperatures [36]. Mass per mass (%) was used to calculate the iron nanoparticle production yield. In the biosynthetic method, 0.4 g of nanoparticles was generated from 100 mL of *Eryngium billardieri* extract, yielding a 0.4% yield. However, 0.6 g of nanoparticles were produced by chemical synthesis employing 1.3336 g of ferrous sulphate heptahydrate, which corresponds to a higher yield of 0.45%. The solution's chilling to near-freezing temperatures slows the reduction process, resulting in smaller, more homogeneous nanoparticles. The magnetic churning guarantees homogeneity while preventing agglomeration. After production, the nanoparticles are rinsed with deionised water and ethanol to remove unreacted salts and byproducts. The drying stage at 80°C eliminates any remaining solvent, leaving the nanoparticles clean and suitable for further functionalisation or application. The nanoparticles formation mechanism is indicated as follows. Iron nanoparticles were synthesized using a reduction process in which Fe²⁺ ions are transformed into Fe⁰ using sodium borohydride (NaBH₄) in aqueous solution. Sodium borohydride initiates the reduction process by contributing electrons to Fe²⁺ ions [37]. The overall reaction is as follows



This process produces zero-valent iron (Fe⁰), which clusters into nanoparticles. The reduction happens at mild conditions, often at room temperature and pH 6, as determined by the system's buffering capability. Sodium borohydride dissociates in water, producing hydroxide ions (OH⁻) that preserve pH and prevent iron nanoparticles from oxidizing excessively [38]. Furthermore, stirring and cooling throughout the reaction facilitate the homogenous creation of Fe nanoparticles, which are subsequently separated using centrifugation, filtration, and drying. This approach ensures a regulated synthesis of iron nanoparticles.

To achieve piperazine encapsulation, the iron nanoparticles were chloro-functionalized [39]. First, 1.5 g of synthesized iron nanoparticles were mixed with 35 mL of toluene. Then, 0.75 mL of 3-chloropropyltrimethoxysilane was added, and the solution was gradually heated to 100°C. The resulting chloro-functionalized iron nanoparticles were separated with neodymium magnets and washed with diethyl ether.

They were then vacuum-dried. 0.05 g of piperazine was then added to 0.9 g of chloro-functionalized iron nanoparticles in 15 mL of toluene. This mixture was stirred at a low rpm for 6 hours. The resulting piperazine-immobilized iron nanoparticles were washed with diethyl ether, then dichloromethane (CH₂Cl₂), and then dried under vacuum. To assure repeatability, the iron nanoparticles were synthesized in triplicate. Each copy was treated under similar conditions, and the resulting nanomaterials were examined for consistency in size, shape, and other parameters, proving their reproducibility throughout several synthesis runs.

Characterization studies

The properties of the prepared *Eryngium billardieri* bioextract, piperazine, *Eryngium billardieri*-synthesized Fe nanoparticles, and piperazine-encapsulated Fe Nanoparticles were characterized using Ultraviolet-visible spectroscopy (UV-Vis) and Fourier Transform Infrared (FTIR) spectroscopic analysis. The samples were analyzed with the Systronics Double Beam - Make UV-Vis spectrophotometer. Each sample was properly diluted in a suitable solvent to ensure it fell within the measurable absorbance range. To correct the baseline, the spectrophotometer was calibrated with a blank solution containing the same solvent as the sample preparation solution. The samples were placed in a quartz cuvette and their absorbance was measured from 200 to 800 nm. The UV-Vis spectra revealed information about the samples' electronic transitions, confirming the presence of specific functional groups and the formation of nanoparticles. FTIR was carried out with the Agilent Cary 630- Make FTIR Spectrometer. Solid samples were prepared by combining with potassium bromide (KBr) and pressing into a pellet, whereas liquid samples were placed on the Attenuated Total Reflectance (ATR) accessory. To ensure accurate measurements, the FTIR spectrometer was calibrated with a background scan that contained no samples. Samples were scanned in the mid-infrared range (4000-400 cm⁻¹) to obtain their Infrared Ray (IR) spectrums. The resulting spectra revealed information about the functional groups present in the samples by identifying distinct absorption bands. The crystalline structure of the prepared *Eryngium billardieri* bioextract, piperazine, *Eryngium billardieri*-synthesized Fe nanoparticles, and piperazine-encapsulated Fe NPs was determined using X-ray diffraction (XRD) testing. The XRD analysis was carried out on the Panalytical X'Pert PRO XRD equipment. To ensure uniformity during testing, the samples were finely ground and evenly distributed on a sample holder. The XRD equipment was calibrated with a standard reference material to ensure accurate measurements. The analysis used a Cu target X-ray source and covered a 2θ range of 10 degrees to 90 degrees with a step count of 0.002 degrees. The samples were exposed to X-rays, and their diffraction patterns were recorded. The diffraction data were used to identify the crystalline phases in the samples and estimate the crystallite size and lattice parameters. This analysis provided detailed information on the crystalline nature of iron nanoparticles and confirmed the successful

encapsulation with piperazine. To characterize the surface morphology and chemical composition of *Eryngium billardieri*-synthesized iron nanoparticles and piperazine-encapsulated iron nanoparticles, Field Emission Scanning Electron microscopy (FE-SEM) and X-ray Photoelectron Spectroscopy (XPS) were performed. The FE-SEM analysis was carried out on the JEOL JSM-7600F machine. To improve conductivity, the samples were sputter-coated with a thin layer of gold prior to FE-SEM analysis. The coated samples were then placed in the FE-SEM chamber, where they were imaged under high vacuum at various magnifications to determine surface morphology and particle size. The images revealed detailed information about the shape, size, and distribution of the nanoparticles. The X-ray photoelectron spectroscopy (XPS) analysis was carried out on the Thermo Scientific K-Alpha XPS system. The samples were loaded into the XPS chamber and exposed to monochromatic Al K α X-rays. The emitted photoelectrons were detected and analyzed to determine the elemental composition and chemical states of the elements found in the samples. XPS spectra were collected over a range of binding energies to determine the presence and oxidation states of elements in both the iron nanoparticles and the encapsulated nanoparticles. The prepared *Eryngium billardieri*-synthesized Fe NPs and piperazine-encapsulated iron nanoparticles were subjected to extensive magnetization studies, including Zero-Field Cooled (ZFC) and Field-Cooled (FC) measurements, as well as hysteresis loop analyses at different temperatures. The Lakeshore 7407 Vibrating Sample Magnetometer (VSM) was used to conduct magnetization studies. The samples were cooled to 100 K, 200 K, and 300 K without an applied magnetic field (ZFC) before being subjected to a magnetic field while cooling (FC). Magnetization was measured as the temperature increased in order to determine the thermal dependence of magnetic properties. Hysteresis loops were created by changing the magnetic field and measuring the resulting magnetization at temperatures of 100, 200, and 300 K. This analysis provided information about the iron nanoparticle's magnetic behavior and coercivity. Alternating Current Magnetic (AC) susceptibility tests were carried out using 4294A Precision Impedance Analyzer. The samples were subjected to alternating magnetic fields with frequencies of 1533 Hz, 5344 Hz, and 9266 Hz. The complex impedance response was measured to determine the frequency dependence of magnetic susceptibility. Integrating these techniques resulted in a thorough understanding of the NPs' magnetic properties and electronic structure.

Scanning electron microscope (SEM), (Make - JEOL JSM-7600F), was used to perform Energy Dispersive X-ray Spectroscopy (EDS). The synthesised iron nanoparticles and piperazine-iron nanoparticles were analyzed by subjecting them to an electron beam, which stimulated the sample and released X-rays, allowing elemental composition to be determined using observed energy peaks. Photoluminescence (PL) spectroscopy was performed using a spectrofluorometer (Make-Nesara Instruments) and a xenon lamp. The nanoparticles were disseminated in deionised water, with the

excitation wavelength set to 350 nm. Emission spectra were acquired between 350 and 600 nm to investigate electron-hole recombination and the enhancement in photocatalytic activity after piperazine encapsulation.

Micromeritics ASAP 2020 analyzer was used to determine the Brunauer-Emmett-Teller (BET) analysis surface area. Dried Fe NPs were vacuum degassed at 150°C for 4 hours. Nitrogen adsorption and desorption isotherms were measured at 77 K. The surface area, pore volume, and pore size distribution were calculated using the BET method.

Batch Degradation Studies

Water infused aniline yellow dye was used to as textile industry effluent. This dye was degraded with *Eryngium billardieri*-synthesized iron nanoparticles and piperazine-encapsulated iron nanoparticles in both dark and in the presence of photocatalytic environments. The dye degradation efficiency was calculated using different aniline yellow dye concentrations, nanoparticles quantity, solution pH, ionic strength, and reaction duration. The equation used to calculate the dye degradation efficiency was as follows:

$$\text{Degradation efficiency \%} = \frac{C_0 - C}{C_0} \text{ -----Eq. 1}$$

In the equation above, C_0 represents the initial concentration and C represents the change in concentration over time. The absorbance variations were measured with a UV-Vis spectrophotometer. The pH of iron nanoparticles in aniline yellow solution was adjusted by adding sodium hydroxide and hydrochloric acid. To determine ionic strength, aniline yellow solution was mixed with sodium chloride and iron nanoparticles. The concentration of sodium chloride was increased from 0.05M to 0.1M, resulting in varying dye degradation efficiencies. UV-Vis spectrometry was used to measure the concentration of residual aniline yellow dye after degradation. Iron nanoparticles were isolated and removed from the solution using neodymium magnets.

Results & Discussions

UV-Vis Analysis

UV-Vis spectrum of *Eryngium billardieri* extract, Piperazine, *Eryngium billardieri* bio-synthesized Fe NPs, Piperazine encapsulated Fe NPs are shown in Figure 1.

Figure 1

The UV-Vis spectrum of *Eryngium billardieri* extract, with an absorbance of 331.24 nm, indicates the presence of flavonoids, which are known for their antioxidant and therapeutic properties. This absorbance wavelength corresponds to the electronic transitions characteristic of these compounds, thereby confirming their presence [40]. Piperazine's UV-Vis spectrum shows an absorbance peak at 263.14 nm, indicating the presence of π - π transitions in conjugated systems. This wavelength is characteristic of aromatic amine structures and indicates piperazine's chemical structure. Such absorption characteristics are consistent with studies conducted by Prabavathi et al. (2015) [41]. The UV-Vis spectrum of *Eryngium billardieri* bio-synthesized iron nanoparticles reveals absorbance peaks at 229.32 nm and 319.83 nm, indicating surface plasmon resonance and electronic transitions. The peak at 229.32 nm corresponds to the surface plasmon resonance effect, whereas the 319.83 nm peak indicates the presence of organic compounds from the plant extract that cover the nanoparticles. This behavior is consistent with findings in recent literature (Pattanayak et al. 2021) [42], which discuss similar spectral features in green-synthesized nanoparticles. The UV-Vis spectrum of Piperazine-encapsulated *Eryngium billardieri* bio-synthesized iron nanoparticles reveals an absorbance peak at 243.19 nm. This peak is likely caused by electronic transitions within the encapsulating piperazine, indicating successful encapsulation and potential modification of the nanoparticle surface properties. [43].

FTIR Analysis

FTIR spectrum of *Eryngium billardieri* extract, Piperazine, *Eryngium billardieri* bio-synthesized iron nanoparticles, Piperazine encapsulated iron nanoparticles are shown in Figure 2.

Figure 2.

The FTIR spectrum of *Eryngium billardieri* extract shows changes near 585 cm^{-1} , indicating C-X bending vibrations, caused by halogenated compounds. Peaks at 1886 cm^{-1} indicate C=O stretching, which is typical for carbonyl groups. Variations near 2125 cm^{-1} and 2432 cm^{-1} were caused by C \equiv N stretching vibrations. The broad variations around 3486 cm^{-1} indicate O-H stretching, which confirms the presence of hydroxyl groups [44]. The FTIR spectrum of piperazine exhibits interesting features: variations at 514 cm^{-1} and 572 cm^{-1} suggest C-N bending vibrations; peaks at 825 cm^{-1} and 981 cm^{-1} are characteristic of N-H bending and C-N stretching; 1110 cm^{-1} and 1245 cm^{-1} indicate C-N stretching vibrations; the band at 1406 cm^{-1} reflects N-H bending; 1546 cm^{-1} corresponds to C=C stretching; 2334 cm^{-1} indicates potential C \equiv N stretching; and broad bands at 2831 cm^{-1} , 3178 cm^{-1} , and 3411 cm^{-1} indicate N-H and C-H stretching [45]. The FTIR spectrum of *Eryngium billardieri* bio-synthesized iron nanoparticles reveals distinct features. Variations at 773 cm^{-1} indicate Fe-O stretching, which is characteristic of iron oxide nanoparticles. Peaks at 1316 cm^{-1} and 1439 cm^{-1} indicate C-H bending and C-N stretching, respectively,

likely due to organic capping agents. The peak at 1727 cm^{-1} indicates C=O stretching, while the broad band at 3483 cm^{-1} represents O-H stretching, indicating hydroxyl groups [46]. The FTIR spectrum of Piperazine-encapsulated iron nanoparticles reveals characteristic peaks. At 539 cm^{-1} , indicating Fe-O vibrations; 1106 cm^{-1} and 1231 cm^{-1} , suggesting C-N stretching and N-H bending from the piperazine structure; 1483 cm^{-1} , corresponding to C-H bending; 1769 cm^{-1} , indicating C=O stretching, possibly due to surface modifications; and a broad band at 3469 cm^{-1} , signifying O-H stretching [47].

X-RD Analysis

XRD spectrum of *Eryngium billardieri* bio-synthesized iron nanoparticles, Piperazine encapsulated iron nanoparticles are shown in Figure 3 (a) & (b) respectively.

Figure 3.

The XRD spectrum of *Eryngium billardieri* bio-synthesized iron nanoparticles reveals peaks at 26.31, 28.29, 39.69, 46.84, 57.41, 71.14, and 76.84 degrees, indicating the nanoparticle's crystalline nature. These peaks correspond to the (110), (200), (211), (220), (310), (222), and (321) planes of face-centered cubic iron, which confirm the formation of iron nanoparticles. [48]. The XRD spectrum of *Eryngium billardieri* bio-synthesized iron nanoparticles shows peaks at 26.31, 28.29, 39.69, 46.84, 57.41, 71.14, and 76.84 degrees, indicating crystalline structure. These peaks correspond to the (110), (200), (211), (220), (310), (222), and (321) planes of face-centered cubic iron, indicating the formation of iron nanoparticles [49].

The oxidation state of Fe in nanoparticles influenced their magnetic properties. Iron oxide nanoparticles, such as Fe_2O_3 (hematite) and Fe_3O_4 (magnetite), exhibited different magnetic behaviors due to their electron configurations [50]. Fe_3O_4 , containing both Fe^{2+} and Fe^{3+} , displayed strong magnetism, while Fe_2O_3 , primarily composed of Fe^{3+} , showed weak magnetism [51]. Since the iron nanoparticles were synthesized at room temperature, partial oxidation likely occurred, resulting in reduced magnetic strength [52]. XRD analysis was done to confirm whether Fe_3O_4 or Fe_2O_3 were formed by identifying characteristic peaks. The absence of Fe_3O_4 peaks suggests limited magnetism due to the dominance of Fe^{3+} species [53].

Field Electron – Scanning Electron Microscopy (FE-SEM)

FE-SEM image of *Eryngium billardieri* bio-synthesized iron nanoparticles, Piperazine encapsulated iron nanoparticles are shown in Figure 4 (a) & (b) respectively.

Figure 4.

Figure 4 (a) depicts a FE-SEM image of *Eryngium billardieri* bio-synthesized iron nanoparticles that are spherical and uniformly distributed, with an average size of 20-30 nm. The surface nanostructures have a smooth morphology, indicating effective bio-reduction and stabilization by plant extracts. These findings are consistent with a recent study conducted by Maghsoudy et al., 2019, which showed similar morphology in bio-synthesized iron nanoparticles, confirming the efficacy of using plant extracts for nanoparticle synthesis [54]. Figure 4(b) shows a FE-SEM image of Piperazine-encapsulated iron nanoparticles that are well-defined and spherical, with an average size of 20-25 nm. Piperazine molecules adsorbed onto the surface of iron nanoparticles, forming a protective layer. This process prevented agglomeration, resulting in smooth and uniform surface nanostructures, which improved stability and dispersibility [55].

XPS analysis

The X-ray photoelectron spectroscopy (XPS) analysis indicated a lot of details regarding the surface chemistry, elemental composition, and electronic structure of the piperazine-encapsulated *Eryngium billardieri* - biosynthesized iron nanoparticles. As shown in Figure 5(a), the survey scan confirms the presence of important elements such as —carbon (C), oxygen (O), iron (Fe), and nitrogen (N)—which together confirm the successful synthesis and piperazine encapsulation. These elemental signals indicates that the encapsulation not only coated the nanoparticle surfaces but also influenced their chemical environment and potential reactivity.

Figure 5(b) shows a high-resolution C1s spectrum with two distinct peaks at 284 eV and 288 eV, corresponding to C-C and C-O bonds, respectively. These peaks represent the incorporation of organic carbon and oxygen-based functional groups produced from piperazine into the nanoparticle surface. Such organic moieties promote colloidal stability and reduce agglomeration, resulting in better nanoparticle dispersion in aqueous systems. These surface alterations also help to reduce surface imperfections, which are common sites of electron-hole recombination. Figure 5(c) reveals a strong signal at 402 eV, indicating CNH (NH₂)₂⁺ and C-N bonds. These nitrogen-containing groups clearly demonstrate piperazine's effective surface incorporation. Importantly, nitrogen doping or surface functionalisation has been shown to reduce charge recombination by modifying the electronic band structure and introducing favorable energy states that enhance charge separation. Thus, the inclusion of nitrogen from piperazine boosted photocatalytic performance by increasing electron lifetimes and promoting more effective redox processes [57].

In Figure 5(d), the O_{1s} spectrum shows a peak at 530 eV, which is consistent with lattice oxygen or oxygen bound in iron oxides/hydroxides. This reveals the presence of Fe-O bonds, which confirms iron

oxidation and phase formation. These oxygen environments are essential for photocatalysis because they participate directly in redox reactions with adsorbed species and aid in charge transfer mechanisms. The iron-oxygen interaction also stabilizes the nanoparticle structure, which is required for long-term catalytic activity. The Fe2p spectrum (Figure 5e) shows a peak at 712 eV, representing Fe²⁺ in the Fe2p_{3/2} area. This validates the divalent oxidation state of iron in nanoparticles. The presence of Fe²⁺, rather than a mixture of Fe²⁺ and Fe³⁺, is crucial because Fe²⁺ ions are more reactive in Fenton-like processes, which play a key role in dye degradation during photocatalytic conditions. The oxidation state effects electron transfer kinetics and the ease with which electrons are collected or released during photochemical processes.

Figure 5.

Magnetic properties

Piperazine-encapsulated bio-synthesized iron nanoparticles's magnetic properties were evaluated in both zero field cooled (ZFC) and field cooled (FC) modes. In ZFC mode, the magnetic moment of Piperazine-encapsulated bio-synthesized iron nanoparticles varies from 30K to 300K, as shown in Fig. 6. As the temperature drops from 300K to 30K, the curve broadens below 80K, with a blocking temperature of around 35K. This broadening indicates that the nanoparticles have transitioned from a superparamagnetic to a blocked state, in which the magnetic moments can no longer freely align due to insufficient thermal energy to overcome the anisotropy energy barriers. Magnetization occurs below 180 Oe as the temperature rises from 30K to 300K, indicating that nanoparticles can respond to external magnetic fields at lower temperatures [60]. In FC mode, under the same magnetic field, the magnetization of the Piperazine-encapsulated bio-synthesized Fe NPs was measured from 300K to 30K, as shown in Fig. 6 (b). Cusp formation at 15K and curve inversion indicate super-paramagnetic nature. This behavior indicates that at lower temperatures, thermal energy is insufficient to randomize the magnetic moments, resulting in a more ordered state. The super-paramagnetic nature of these nanoparticles is critical for biomedical and data storage applications because it enables high magnetic responsiveness without permanent magnetization. The observed magnetic behavior is due to the encapsulation of iron nanoparticles with Piperazine, which stabilizes them and prevents agglomeration, allowing for more precise magnetic interactions. The transition from superparamagnetic to blocked states, as well as the distinct magnetic responses in ZFC and FC modes, is characteristic of fine iron nanoparticles. Encapsulated nanoparticles exhibit high magnetic susceptibility and low coercivity, making them ideal for a variety of technological applications [61].

Figure 6.

Figure 6 (c) shows hysteresis loops recorded at various temperatures to confirm superparamagnetic behavior in Piperazine-encapsulated bio-synthesized iron nanoparticles. The hysteresis loops at 100K, 200K, and 300K show negligible coercivity and remanence, indicating that the nanoparticles do not retain magnetization after being removed from the external magnetic field. This behavior is characteristic of superparamagnetism, in which thermal fluctuations are enough to randomly reorient the magnetic moments of individual nanoparticles, preventing permanent magnetization. At 100K, the loop becomes slightly more pronounced, indicating some blocking behavior caused by reduced thermal energy, which is insufficient to fully randomize magnetic moments. As the temperature rises to 200K and 300K, the loops narrow and become more linear, indicating that the nanoparticles exhibit superparamagnetic behavior at higher temperatures. This temperature dependence is consistent with the properties of superparamagnetic nanoparticles, where higher temperatures promote thermal agitation, resulting in lower coercivity and remanence [62]. The encapsulation of iron nanoparticles with Piperazine improves their stability and prevents agglomeration, resulting in uniform size distribution and consistent magnetic properties. The observed superparamagnetic behavior is consistent with iron nanoparticles that are well-dispersed and small in size, and are highly responsive to external magnetic fields without retaining residual magnetization [63]. The spin behavior of the prepared nanoparticles was studied by measuring their AC susceptibility under an applied magnetic field of 1 Oe at three different frequencies: 1533 Hz, 5344 Hz, and 9266 Hz, from 10K to 80K, as shown in Fig. 6 (d). The AC susceptibility variations show maxima near the blocking temperature for all three frequencies, indicating a transition from superparamagnetic to blocked state. This behavior is consistent with superparamagnetic nanoparticles, in which magnetic moments are free to align with the field above the blocking temperature but freeze below it because thermal energy is insufficient to overcome anisotropy energy barriers [64]. At all frequencies (1533 Hz, 5344 Hz, and 9266 Hz), the AC susceptibility peaks at the blocking temperature, reflecting the frequency dependence of spin relaxation dynamics. Higher frequencies correspond to faster probing of the magnetic relaxation processes, resulting in shifts in the susceptibility peaks. The similarity in the curve patterns across different frequencies and their resemblance to field cooled mode magnetic moment variations suggest that the NPs exhibit consistent spin dynamics and magnetic behavior [65].

EDS Studies

EDS spectrum of *Eryngium billardieri* bio-synthesized iron nanoparticles and Piperazine encapsulated iron nanoparticles are shown in Figure 7 (a) and (b) respectively.

Figure 7

Figure 7(a) depicts the EDS spectrum of *Eryngium billardieri*-synthesized iron nanoparticles, which verifies the presence of elemental iron as the primary component, as well as minor oxygen peaks indicating surface oxidation [66]. Figure 7(b) exhibits the EDS spectrum of piperazine-encapsulated iron nanoparticles, which shows Fe peaks alongside excess chlorine. These correspond to piperazine and chloro-functionalization, which demonstrate excellent encapsulation and surface modification, hence enhancing nanoparticle stability and catalytic activity.

Photoluminescence (PL) spectroscopy

The Photoluminescence (PL) spectra of *Eryngium billardieri* bio-synthesized iron nanoparticles and Piperazine encapsulated iron nanoparticles are shown in Figure 8 (a) and (b) respectively.

Figure 8

Figure 8 shows the photoluminescence (PL) spectra, which provide information about the electron-hole recombination kinetics of the synthesized iron nanoparticles. The unaltered iron nanoparticles synthesized with *Eryngium billardieri* extract have modest emission intensity, indicating a higher rate of electron-hole recombination, which affects photocatalytic effectiveness. In contrast, piperazine-encapsulated Fe nanoparticles have substantially reduced PL intensity, indicating a strong inhibition of electron-hole recombination. This suggests improved charge carrier separation, which is critical for effective photocatalysis. The lower recombination corresponds directly to the enhanced photocatalytic degradation efficiency seen in the enclosed system. Piperazine most likely functions as a surface passivating and stabilizing agent, preventing fast electron-hole annihilation. Such behavior is consistent with the goal of creating materials with higher photoreactivity and stability [67].

BET analysis

The variations in volume adsorbed with relative pressure for *Eryngium billardieri* bio-synthesized iron nanoparticles and Piperazine encapsulated iron nanoparticles are shown in Figure 9 (a) and (b) respectively. Similarly, the fluctuations in pore radius for *Eryngium billardieri* bio-synthesized iron nanoparticles and Piperazine encapsulated iron nanoparticles are shown in Figure 9 (c) and (d) respectively.

Figure 9

The BET study of *Eryngium billardieri*-synthesized iron nanoparticles (Figure 9(a) and 9(c)) shows a type IV isotherm with a hysteresis loop, indicating mesoporous properties. The adsorption-desorption curve indicates capillary condensation within pores, with pore sizes largely in the mesoporous region (2-50 nm).

Figure 9 (c) displays a peak in the pore size distribution, which supports the mesoporous nature. The isotherm remains type IV after piperazine encapsulation (Figure 9(b) and 9(d)), however there is a modest drop in adsorption capacity, indicating partial pore blockage or surface alteration [68]. The shift in the pore size distribution curve (Figure 9 (d)) indicates a reduction in average pore diameter, most likely due to piperazine occupying certain pore spaces. Overall, piperazine encapsulation reduced pore volume and surface area, improving nanoparticle stability while retaining mesoporous characteristics [69] appropriate for catalytic applications.

High Resolution Transmission Electron Microscopy (HRTEM) studies

The HRTEM images of *Eryngium billardieri* bio-synthesized iron nanoparticles and Piperazine encapsulated iron nanoparticles are shown in Figure 10 (a) and (b) respectively.

Figure 10

The HRTEM study of *Eryngium billardieri*-synthesized iron nanoparticles (Figure 10(a)) showed uniformly distributed nanoparticles with a spherical morphology and an average size of 10 to 30 nm. The lattice fringes reveal a crystalline structure, verifying the creation of zero-valent iron (Fe^0) nanoparticles [70]. The absence of agglomeration indicates that the bioactive components in the plant extract serve as stabilizers, preventing particle coalescence. Figure 10(b) indicates HRTEM image of piperazine-encapsulated *Eryngium billardieri*-synthesized iron nanoparticles with a core-shell structure and a thin homogeneous organic layer surrounding the metallic core. This encapsulating layer is due to piperazine functionalisation, which improves nanoparticle stability, inhibits oxidation, and minimizes aggregation [71]. The core-shell architecture demonstrates successful surface modification, which improves dispersibility and catalytic effectiveness, making piperazine-coated nanoparticles more efficient in dye degradation.

Batch Experiments

Degradation of aniline yellow dye using biosynthesized iron nanoparticles and Piperazine encapsulated *Eryngium billardieri* biosynthesized iron nanoparticles were done. Five sets of batch experiments were conducted such as varying iron nanoparticle quantity, initial dye concentration, reaction duration, ionic strength and solution pH. The five sets of degradation experiments were conducted in the presence of sunlight and in dark. While varying one parameter, others were maintained as constant. UV-Vis spectrum analysis of the *Eryngium billardieri* biosynthesized iron nanoparticles and piperazine-encapsulated iron nanoparticles on the aniline yellow dye is shown in Figure 11.

Figure 11

The UV-Vis spectroscopy results indicated different absorbance patterns for the two nanoparticle systems during dye degradation. The green line, which represents piperazine-encapsulated iron nanoparticles, showed a faster fall in the distinctive absorbance peak of aniline yellow dye, indicating higher degradation efficiency. This enhanced performance is ascribed to piperazine's involvement in stabilizing iron nanoparticles, minimizing aggregation [72], and facilitating electron transport in the chlorinated environment, resulting in faster dye degradation. The yellow line, representing Eryngium billardieri-synthesized iron nanoparticles without piperazine, demonstrated a slower decline in dye absorbance, indicating lower catalytic efficacy due to probable nanoparticle aggregation and reduced surface area for dye interaction [73].

Varying the quantity of iron nanoparticles

The amount of iron nanoparticles used in the dye degradation studies ranged between 1000 mg and 2500 mg (Figure 12 (a)). Other parameters were kept constant, including the initial dye concentration of 225 mg/l, the reaction duration of 250 minutes, the ionic strength of 0.09 M, and the solution pH of 9. The dye degradation efficiency varied according to the amount of iron nanoparticles used. The efficiency of Piperazine-encapsulated iron nanoparticles in a dark environment increased from 71% at 1000 mg/l to 92% at 2500 mg/l. Under photo catalytic conditions, the same nanoparticles demonstrated an increase in efficiency from 75% to 96%. In comparison, untreated biosynthesized iron nanoparticles showed lower degradation efficiencies, beginning at 51% in the dark and 55% under photo catalytic conditions at 1000 mg/l and increasing to 79% and 81%, respectively, at 2500 mg/l. The larger surface area provided for catalytic reactions can explain the increase in dye degradation efficiency with higher concentrations of iron nanoparticles. Iron nanoparticles accelerate the degradation process by catalyzing redox reactions that break down dye molecules into simpler products. Piperazine encapsulation enhances the stability and dispersibility of iron nanoparticles, resulting in improved interaction with dye molecules and higher degradation efficiencies. This encapsulation also improves the nanoparticle's ability to use light energy in photocatalytic environments, as light excites electrons in the iron nanoparticles, resulting in electron-hole pairs that participate in redox reactions [74].

Varying initial concentration of aniline yellow dye

Dye degradation experiments were carried out by varying the initial dye concentration from 150 mg/l to 300 mg/l (Figure 12 (b)) while holding other parameters constant: Fe nanoparticle quantity at 1750 mg/l, reaction duration at 250 min, ionic strength at 0.09 M, and solution pH at 9. The dye degradation efficiency varied significantly with initial dye concentration. The efficiency of Piperazine-encapsulated iron nanoparticles in a dark environment increased from 61% at 150 mg/l to 91% at 300 mg/l. Under

photocatalytic conditions, the same nanoparticles demonstrated an increase in efficiency from 68% to 95%. In comparison, untreated biosynthesized iron nanoparticles demonstrated lower degradation efficiencies, beginning at 49% in the dark and 54% under photo catalytic conditions at 150 mg/l and increasing to 71% and 79%, respectively, at 300 mg/l. The observed increase in dye degradation efficiency with higher initial dye concentrations can be attributed to the availability of more dye molecules to interact with the iron nanoparticles. These nanoparticles act as catalysts, accelerating the degradation process by redox reactions that break down dye molecules into less complex and less harmful products [75].

Varying the reaction duration

The reaction duration was varied from 160 to 340 minutes in order to study dye degradation (Figure 12 (c)). Other parameters, such as the quantity of iron nanoparticles (1750 mg/l), the initial dye concentration (225 mg/l), the ionic strength (0.09 M), and the solution pH (9), were held constant. Longer reaction times resulted in increased dye degradation efficiency. The efficiency of Piperazine-encapsulated iron nanoparticles in a dark environment increased from 55% at 160 minutes to 91% at 340 minutes. Under photocatalytic conditions, the efficiency rose from 57% to 94%. In comparison, untreated biosynthesized iron nanoparticles demonstrated lower degradation efficiencies, beginning at 44% in the dark and 53% under photocatalytic conditions at 160 min and increasing to 81% and 85%, respectively, at 340 min. The observed trend can be explained by the fact that longer reaction times allow the iron nanoparticles to interact with dye molecules, resulting in more complete degradation. The iron nanoparticles accelerate the degradation process by catalyzing redox reactions, which break down dye molecules into simpler and less harmful products [76].

Varying ionic strength of the solution

Dye degradation experiments were carried out by varying the ionic strength from 0.03 M to 0.15 M (Figure 12 (d)) while holding other parameters constant: Fe nanoparticle quantity at 1750 mg/l, initial dye concentration at 225 mg/l, reaction duration at 250 minutes, and solution pH at 9. The dye degradation efficiency increased significantly with increasing ionic strength. Piperazine-encapsulated iron nanoparticles in a dark environment increased efficiency from 49% at 0.03 M to 90% at 0.15 M. Under photo catalytic conditions, the efficiency rose from 55% to 92%. In comparison, untreated biosynthesized iron nanoparticles demonstrated lower degradation efficiencies, beginning at 41% in the dark and 44% under photo catalytic conditions at 0.03 M and increasing to 79% and 82%, respectively, at 0.15 M. Higher ionic strength leads to increased electrostatic interactions between dye molecules and nanoparticles, which increases dye degradation efficiency. Higher ionic strength reduces the repulsive

forces between negatively charged dye molecules and iron nanoparticles, allowing for closer interaction and more efficient catalytic degradation [77].

Figure 12

Varying the pH of the solution

Dye degradation experiments were carried out by varying the pH of the solution from 3 to 14, while keeping the other parameters constant: iron nanoparticle quantity at 1750 mg/l, initial dye concentration at 225 mg/l, reaction duration at 250 minutes, and ionic strength at 0.09 M. The efficiency of dye degradation varied significantly with pH level. The efficiency of Piperazine-encapsulated iron nanoparticles in a dark environment decreased from 87% at pH 3 to 55% at pH 14. Under photo catalytic conditions, the efficiency varied from 91% at pH 3 to 61% at pH 14. Similarly, untreated biosynthesized iron nanoparticles demonstrated lower degradation efficiencies, beginning at 81% in the dark and 84% under photo catalytic conditions at pH 3, then decreasing to 43% and 53%, respectively, at pH 14. The observed trend is explained by pH's effect on the surface charge and stability of iron nanoparticles, as well as the dye molecules' ionisation state. At lower pH levels, the iron nanoparticles are more positively charged, which improves their interaction with negatively charged dye molecules and results in higher degradation efficiencies. As the pH rises, the nanoparticle's surface charge becomes less positive or even negative, reducing their interaction with dye molecules and decreasing degradation efficiency [78]. The present investigation has been compared with significant previous literatures and the comparative study is shown in Table 2.

Table 2 – Comparison of the present study with other literatures

Study	Nanomaterial	Synthesis Method	Photocatalytic Activity	Key Findings
Present Study	Iron nanoparticles	Green synthesis using <i>Eryngium billardieri</i> extract	Photocatalytic degradation of dyes (to be tested)	Bio-synthesized iron nanoparticles showed promising results for photocatalysis, though further optimization is needed for efficiency.
Thakur et al. (2024) [79]	Anatase and rutile TiO ₂ nanoparticles	Chemical and environmentally friendly methods	Enhanced photocatalytic activity, antibacterial, and antioxidant properties	TiO ₂ nanoparticles displayed improved performance with doping methods, particularly in photocatalysis and wastewater treatment.
Devi et al. (2024) [80]	Zn and Gd-doped MnO nanoparticles	Green synthesis using <i>Pinus roxburghii</i> extract	Antifungal, antibacterial, and antioxidant activities	Zn and Gd-doped MnO nanoparticles showed excellent antimicrobial properties,

				indicating potential for environmental applications.
Thakur & Thakur (2024) [26]	Co-Ni-doped TiO ₂ nanoparticles	Green and chemical methods	Photodegradation of methyl orange and methylene blue	Co-Ni-doped TiO ₂ nanoparticles demonstrated 100% degradation of dyes under UV light, showcasing their efficiency in textile wastewater treatment.

The primary importance of this work is its innovative application of *Eryngium billardieri* extract for the environmentally friendly production of iron nanoparticles, which is comparatively untapped in contrast to materials like TiO₂ and ZnO that are extensively researched. Although doped TiO₂ (Thakur et al., 2024 [79]; Thakur & Thakur, 2024 [26]) or MnO nanoparticles (Devi et al., 2024 [80]) have shown excellent photocatalytic or antimicrobial performance in earlier studies, this work presents an environmentally friendly, plant-based method to synthesize iron nanoparticles with a similar potential for dye degradation.

This research broadens the material base by investigating iron nanoparticles produced via a sustainable technique, in contrast to earlier publications that mainly concentrate on TiO₂-based materials. The piperazine-encapsulated Fe NPs, created via a green technique, show promise for biomedical applications such as targeted medication delivery and environmental remediation. The physicochemical characteristics of the piperazine-encapsulated Fe NPs made with *Eryngium billardieri* extract, including improved stability, magnetic responsiveness, and high photocatalytic effectiveness, make them appropriate for a variety of biological uses. Their capacity to operate efficiently in chlorinated settings points to a great deal of promise for targeted drug administration, especially in cancer treatment, where controlled release and site-specific activity are essential. Magnetic-guided delivery systems or magnetic hyperthermia can benefit from the reported magnetic characteristics. Furthermore, their effectiveness as antioxidants and antimicrobials is demonstrated by their large surface area and the production of reactive oxygen species when exposed to light. Because of the low toxicity and biocompatibility guaranteed by the green production, the nanoparticles are safer for use in biological interactions. The design of next-generation nanomedicine tools based on environmentally benign and scalable fabrication techniques is advanced by these findings, which pave the way for the development of multifunctional nanomaterials that can simultaneously diagnose and treat conditions (theranostics), control infections, and deliver drugs. To improve their stability and selectivity for use in biomedical and environmental applications, future studies could concentrate on surface fictionalization of the piperazine-encapsulated iron nanoparticles using biocompatible polymers or ligands. Investigating the impact of adding hybrid nanocomposites or doping with extra metal ions may enhance photocatalytic effectiveness and magnetic behavior even more.

Nanoparticle size and shape can be optimized for improved performance by sophisticated reaction control techniques, such as adjusting the synthesis temperature, pH, and precursor ratios. To assess their practical applicability, long-term stability studies in physiological and environmental settings are necessary. Furthermore, evaluating these nanoparticle's cytotoxicity and biocompatibility in in-vivo models may confirm their safety for use in therapeutic settings.

Conclusions

This study demonstrates that piperazine-encapsulated, *Eryngium billardieri*-mediated iron nanoparticles have substantial potential as efficient catalysts for the breakdown of aniline yellow color. Piperazine's involvement in enhancing reactivity and electron transfer efficiency is highlighted by the improvement in catalytic performance under both dark and photocatalytic conditions, particularly the 96% degradation attained under light exposure. The sensitivity of the degradation process to external conditions was proven by a systematic adjustment of operating parameters, confirming the necessity of precise control in real-world applications. Along with their superparamagnetic characteristics and spin dynamics, the particles' structural integrity, mesoporous nature, and nanoscale homogeneity all point to good dispersibility, recyclability, and applicability in magnetically recoverable systems. Crucially, the observed magnetic behaviour adds another level of process tunability, particularly for systems that need external-field-driven recovery or targeted control. Collectively, these observations lend credence to the application of such hybrid nanocatalysts in environmentally friendly, scalable wastewater treatment systems..

References

1. C.R. Holkar, A.J. Jadhav, D.V. Pinjari, N.M. Mahamuni, A.B. Pandit, J. Environ. Manage. 182 (2016) 351-366. <https://doi.org/10.1016/j.jenvman.2016.07.090>
2. S. Sudarshan, S. Harikrishnan, G. RathiBhuvaneswari, V. Alamelu, S. Aanand, A. Rajasekar, M. Govarthan, J. Appl. Microbiol. 134 (2023) lxac064. <https://doi.org/10.1093/jambio/lxac064>
3. A. Srivastava, R.M. Rani, D.S. Patle, S. Kumar, J. Chem. Technol. Biotechnol. 97 (2022) 26-41. <https://scijournals.onlinelibrary.wiley.com/doi/epdf/10.1002/jctb.6891>
4. M. Behera, J. Nayak, S. Banerjee, S. Chakraborty, S.K. Tripathy, J. Environ. Chem. Eng. 9 (2021) 105277. <https://doi.org/10.1016/j.jece.2021.105277>
5. M.T. Islam, T. Islam, T. Islam, M.R. Repon, Text. Leather Rev. 5 (2022) 327-373. <https://doi.org/10.31881/TLR.2022.27>

6. P. Moradihamedani, Polym. Bull. 79 (2022) 2603-2631. <https://doi.org/10.1007/s00289-021-03603-2>
7. J. Chaudhary, G. Tailor, M. Yadav, C. Mehta, Biocatal. Agric. Biotechnol. 50 (2023) 102692. <https://doi.org/10.1016/j.bcab.2023.102692>
8. H. Liu, C. Wang, G. Wang, Chem. - Asian J. 15 (2020) 3239-3253. <https://doi.org/10.1002/asia.202000895>
9. K. Fedorov, K. Dinesh, X. Sun, R. D. C. Soltani, Z. Wang, S. Sonawane, G. Boczkaj, Chem. Eng. J. 432 (2022) 134191. <https://doi.org/10.1016/j.cej.2021.134191>
10. N. Shreyash, S. Bajpai, M.A. Khan, Y. Vijay, S.K. Tiwary, M. Sonker, ACS Appl. Nano Mater. 4 (2021) 11428-11457. <http://doi.org/10.1021/acsnm.1c02946>
11. A. Hosseingholian, S.D. Gohari, F. Feirahi, F. Moammeri, G. Mesbahian, Z.S. Moghaddam, Q. Ren, Mater. Today Sustain. 1 (2023) 100500. <https://doi.org/10.1016/j.mtsust.2023.100500>
12. J.A. Aboyewa, N.R. Sibuyi, M. Meyer, O.O. Oguntibeju, Plants 10 (2021) 1929. <https://doi.org/10.3390/plants10091929>
13. S.A. Akintelu, A.S. Folorunso, F.A. Folorunso, A.K. Oyebamiji, Heliyon 6(7) (2020) e04508. <https://doi.org/10.1016/j.heliyon.2020.e04508>
14. A.M. Alswieleh, ACS Appl. Polym. Mater. 5 (2023) 1334-1343. <http://doi.org/10.1021/acsapm.2c01852>
15. P.A. Atmianlu, R. Badpa, V. Aghabalaei, M. Baghdadi, J. Environ. Chem. Eng. 9 (2021) 106514. <http://doi.org/10.1016/j.jece.2021.106514>
16. P. Kumar, A. Kaushik, S. Kumar, N. Thakur, Phys. Scr. 99 (2024) 105960. <https://doi.org/10.1088/1402-4896/ad7329>
17. S. Sharma, M. Devi, P. Kumar, N. Thakur, K. Kumar, K. Jeet, N. Thakur, Toxicol. Environ. Chem. 107 (2025) 178–206. <https://doi.org/10.1080/02772248.2024.2448952>
18. P. Kumar, V. Arya, A. Kumar, N. Thakur, Int. J. Mater. Res. 116 (2025) 30–49. <https://doi.org/10.1515/ijmr-2023-0343>
19. N. Verma, D. Pathak, K. Kumar, K. Jeet, S. Nimesh, L. Loveleen, N. Thakur, Mater. Chem. Phys. 333 (2025) 130422. <https://doi.org/10.1016/j.matchemphys.2024.130422>

20. M. Devi, S. Sharma, P. Kumar, N. Thakur, G. Kumar, M.V. Sharma, N. Thakur, *Colloids Surf. C Environ. Asp.* 2 (2024) 100046. <https://doi.org/10.1016/j.colsurfc.2024.100046>
21. P. Kumar, S. Kumar, A. Tapwal, S. Nimesh, N. Thakur, *Sustain. Chem. Environ.* 8 (2024) 100160. <https://doi.org/10.1016/j.rsce.2024.100160>
22. S. Thakur, P. Kumar, N. Thakur, K. Kumar, K. Jeet, S. Kumar, N. Thakur, *J. Indian Chem. Soc.* 101199 (2024). <https://doi.org/10.1016/j.jics.2024.101199>
23. P. Kumar, N. Thakur, K. Kumar, S. Kumar, A. Dutt, V.K. Thakur, N. Thakur, *Coord. Chem. Rev.* 507 (2024) 215750. <https://doi.org/10.1016/j.ccr.2024.215750>
24. A. Rana, P. Kumar, N. Thakur, S. Kumar, K. Kumar, N. Thakur, *Nano-Struct. Nano-Objects* 38 (2024) 101188. <https://doi.org/10.1016/j.nanoso.2024.101188>
25. R. Kumar, S. Kaushal, N. Verma, P. Kumar, N. Thakur, A. Kumar, N. Thakur, *J. Mol. Liq.* 126254 (2024). <https://doi.org/10.1016/j.molliq.2024.126254>
26. N. Thakur, N. Thakur, *J. Mater. Sci. Mater. Electron.* 35 (2024) 134. <https://doi.org/10.1007/s10854-023-11851-3>
27. P. Kumar, D. Pathak, N. Thakur, *Emerg. Mater.* (2024) 1-17. <https://doi.org/10.1007/s42247-024-00742-w>
28. P. Kumar, A. Tapwal, S. Kumar, N. Thakur, *Adv. Nat. Sci. Nanosci. Nanotechnol.* 15 (2024) 025014. <https://doi.org/10.1088/2043-6262/ad50bb>
29. N. Thakur, P. Kumar, *Int. J. Nanosci.* 23 (2024) 2450010. <https://doi.org/10.1142/S0219581X24500108>
30. N. Verma, D. Pathak, N. Thakur, *Next Mater.* 5 (2024) 100271. <https://doi.org/10.1016/j.nextmat.2024.100271>
31. N. Thakur, P. Kumar, *Int. J. Nanosci.* 23 (2024) 2450010. <https://doi.org/10.1142/S0219581X24500108>
32. N. Thakur, N. Thakur, K. Kumar, V. Arya, A. Kumar, S. Kalia, *Biomater. Polym. Horiz.* 1 (2022) Article 330. <https://www.ojs.bdtopten.com/33015.eaapublishing/index.php/bph/article/view/330>

33. N. Thakur, N. Thakur, J. Dispersion Sci. Technol. (2024) 1–16. <https://doi.org/10.1080/01932691.2024.2312841>
34. A. Balkrishna, N. Thakur, B. Patial, S. Sharma, A. Kumar, V. Arya, R. Amarowicz, Processes 11 (2023) 1479. <https://doi.org/10.3390/pr11051479>
35. M.S. Daneshzadeh, H. Abbaspour, L. Amjad, A.M. Nafchi, J. Food Meas. Charact. 14 (2020) 708-715. <https://doi.org/10.1007/s11694-019-00317-y>
36. I.A. Radini, N. Hasan, M.A. Malik, Z. Khan, J. Photochem. Photobiol. B: Biol. 183 (2018) 154-163. <https://doi.org/10.1016/j.jphotobiol.2018.04.014>
37. S.H. Nguyen, N.T. Vu, H. Van Nguyen, B. Nguyen, T.T. Luong, Environ. Sci. Nano (2025). <https://doi.org/10.1039/D4EN00843J>
38. L. Xu, H.W. Liang, Y. Yang, S.H. Yu, Chem. Rev. 118 (2018) 3209-3250. <https://doi.org/10.1021/acs.chemrev.7b00208>
39. M. Chadha, A. Garg, A. Bhalla, S. Berry, Tetrahedron 150 (2023) 133741. <https://doi.org/10.1016/j.tet.2023.133741>
40. M. Kikowska, M. Dworacka, I. Kędziora, B. Thiem, Rev. Bras. Farmacogn. 26 (2016) 392-399. <https://doi.org/10.1016/j.bjp.2016.01.008>
41. S. SenGupta, N. Maiti, R. Chadha, S. Kapoor, Chem. Phys. 436 (2014) 55-62. <https://doi.org/10.1016/j.chemphys.2014.03.011>
42. D.S. Pattanayak, D. Pal, C. Thakur, S. Kumar, G.L. Devnani, Mater. Today: Proc. 44 (2021) 3150-3155. <http://doi.org/10.1016/j.matpr.2021.02.821>
43. H.N. Prasad, A.P. Ananda, S. Sumathi, K. Swathi, K.J. Rakesh, H.S. Jayanth, P. Mallu, J. Mol. Struct. 1268 (2022) 133683. <https://doi.org/10.1016/j.molstruc.2022.133683>
44. H. Feizi, N. Mollania, H. Mollania, F. Mollania, Research Square (2022) PPR581050 <http://doi.org/10.21203/rs.3.rs-2338838/v1>
45. K. Subashini, S. Periandy, J. Mol. Struct. 1134 (2017) 157-170. <https://doi.org/10.1016/j.molstruc.2016.12.048>
46. N. Sidkey, Al-Azhar, J. Pharm. Sci. 62(2) (2020) 164-179. <http://doi.org/10.21608/ajps.2020.118382>

47. K. Velsankar, G. Parvathy, S. Mohandoss, M. Krishna Kumar, S. Sudhahar, *J. Nanostruct. Chem.* 12 (2021) 625-640. <https://doi.org/10.1007/s40097-021-00434-5>
48. M. Kaur, D.S. Chopra, *Glob. J. Nanomed.* 4(4) (2018) 68-76. <http://doi.org/10.19080/GJN.2018.04.555643><https://doi.org/>
49. M. Mahdavi, F. Namvar, M.B. Ahmad, R. Mohamad, *Molecules* 18(5) (2013) 5954-5964. <https://doi.org/10.3390/molecules18055954>
50. R. Duglet, D. Sharma, V. Singh, D. Sharma, M. Singh, *Solid State Commun.* 396 (2025) 115761. <https://doi.org/10.1016/j.ssc.2024.115761>
51. A.R. Pradipta, A. Irunsa, *Indones. J. Chem. Stud.* 1 (2022) 8-12. <https://doi.org/10.55749/ijcs.v1i1.7>
52. T. Zhang, X. Jin, G. Owens, Z. Chen, *J. Colloid Interface Sci.* 594 (2021) 398-408. <https://doi.org/10.1016/j.jcis.2021.03.065>
53. R. Foroutan, R. Mohammadi, A. Ahmadi, G. Bikhbar, F. Babaei, B. Ramavandi, *Chemosphere* 286 (2022) 131632. <https://doi.org/10.1016/j.chemosphere.2021.131632>
54. N. Maghsoudy, P.A. Azar, M.S. Tehrani, S.W. Husain, K. Larijani, *J. Nanostruct. Chem.* 9 (2019) 203-216. <http://doi.org/10.1007/s40097-019-0311-z>
55. A. Ropp, R. F. André, S. Carencó, *ChemPlusChem* 88(11) (2023) e202300469. <https://doi.org/10.1002/cplu.202300469>
56. N.H. Anh, D.V. Nguyen, T.A. Luu, P.D.M. Phan, H.P. Toan, P.P. Ly, H.T. Vuong, *Sol. RRL* 8 (2024) 2400034. <http://dx.doi.org/10.1002/solr.202400034>
57. C.C. Ong, R. Jose, M.S.M. Saheed, *Chem. Eng. J.* 388 (2020) 124306. <https://doi.org/10.1016/j.cej.2020.124306>
58. C.J. Weststrate, D. Sharma, D. Garcia Rodriguez, M.A. Gleeson, H.O. Fredriksson, J.W. Niemantsverdriet, *Nat. Commun.* 11 (2020) 750. <https://doi.org/10.1038/s41467-020-14613-5>
59. P. Nagaraju, C. Srilakshmi, N. Pasha, N. Lingaiah, I. Suryanarayana, P.S. Prasad, *Appl. Catal. A Gen.* 334 (2008) 10-19. <https://doi.org/10.1016/j.apcata.2007.04.024>

60. M. Chandran, D. Yuvaraj, L. Christudhas, K.V. Ramesh, *Biotechnol. Indian J.* 12(12) (2016) 112. <https://www.tsijournals.com/articles/biosynthesis-of-iron-NPs-using-the-brown-seaweed-dictyota-dicotoma.html>
61. E. Alphandéry, *Int. J. Pharm.* 586 (2020) 119472. <https://doi.org/10.1016/j.ijpharm.2020.119472>
62. A. Miri, H. Najafzadeh, M. Darroudi, M.J. Miri, M.A.J. Kouhbanani, M. Sarani, *ChemistryOpen* 10(3), (2021), 327-333. <https://doi.org/10.1002/open.202000186>
63. N. Kobylinska, D. Klymchuk, A. Shakhovsky, O. Khainakova, Y. Ratushnyak, V. Duplij, N. Matvieieva, *RSC Adv.* 11(43) (2021) 26974-26987. <http://doi.org/10.1039/D1RA04080D>
64. T. Suneetha, S. Kundu, S.C. Kashyap, H.C. Gupta, T.K. Nath, *J. Nanosci. Nanotechnol.* 13(1) (2013) 270-278. <https://doi.org/10.1166/jnn.2013.7092>
65. M. Kin, H. Kura, T. Ogawa. *AIP Adv.* 6(12) (2016) 125013. <https://doi.org/10.1063/1.4972059>
66. T. Wang, X. Jin, Z. Chen, M. Megharaj, R. Naidu, *Sci. Total Environ.* 466 (2014) 210-213. <https://doi.org/10.1016/j.scitotenv.2013.07.022>
67. A. Rufus, N. Sreeju, D. Philip, *J. Phys. Chem. Solids* 124 (2019) 221-234. <https://doi.org/10.1016/j.jpcs.2018.09.026>
68. J. Xu, D. Bhattacharyya, *Ind. Eng. Chem. Res.* 46 (2007) 2348-2359. <https://doi.org/10.1021/ie0611498>
69. L. Zhou, Y. He, S. Gou, Q. Zhang, L. Liu, L. Tang, M. Duan, *Chem. Eng. J.* 383 (2020) 123190. <https://doi.org/10.1016/j.cej.2019.123190>
70. C. Rodríguez-Rasero, V. Montes-Jimenez, M.F. Alexandre-Franco, C. Fernández-González, J. Píriz-Tercero, E.M. Cuerda-Correa, *Water* 16 (2024) 1607. <https://doi.org/10.3390/w16111607>
71. W. Zhou, J. Zhu, C. Cheng, J. Liu, H. Yang, C. Cong, T. Yu, *Energy Environ. Sci.* 4 (2011) 4954-4961. <https://doi.org/10.1039/C1EE02168K>
72. Y. Mansourpanah, A. Rahimpour, M. Tabatabaei, L. Bennett, *Desalination* 419 (2017) 79-87. <https://doi.org/10.1016/j.desal.2017.06.006>
73. Y. Wang, T. Xiao, S. Zuo, J. Wan, Z. Yan, B. Zhu, X. Zhang, *J. Hazard. Mater.* 446 (2023) 130698. <https://doi.org/10.1016/j.jhazmat.2022.130698>

74. M.A. Ahmed, E.E. El-Katori, Z.H. Gharni, J. Alloys Compd. 553 (2013) 19-29. <https://doi.org/10.1016/j.jallcom.2012.10.038>
75. M. Nemiwal, T.C. Zhang, D. Kumar, Sci. Total Environ. 767 (2021) 144896. <http://doi.org/10.1016/j.scitotenv.2020.144896>
76. I. Anastopoulos, A. Hosseini-Bandegharai, J. Fu, A.C. Mitropoulos, G.Z. Kyzas, J. Dispersion Sci. Technol. 39(6) (2018) 836-847. <http://doi.org/10.1080/01932691.2017.1398661>
77. M. Arellano-Cortaza, E. Ramírez-Morales, U. Pal, G. Pérez-Hernández, L. Rojas-Blanco, Ceram. Int. 47(19) (2021) 27469-27478. <http://doi.org/10.1016/j.ceramint.2021.06.170>
78. S.H. Ribut, C.A.C. Abdullah, M. Mustafa, M.Z.M. Yusoff, S.N.A. Azman. Mater. Res. Express 6(2) (2018) 025016. <http://doi.org/10.1088/2053-1591/aaecbc>
79. M. Devi, S. Sharma, P. Kumar, N. Thakur, G. Kumar, M.V. Sharma, N. Thakur, Colloids Surf. C Environ. Asp. 2 (2024) 100046. <https://doi.org/10.1016/j.colsuc.2024.100046>
80. N. Thakur, N. Thakur, A. Kumar, V.K. Thakur, S. Kalia, V. Arya, G.Z. Kyzas, Sci. Total Environ. 169815 (2024). <https://doi.org/10.1016/j.scitotenv.2023.169815>

Figures

Figure 1. Ultraviolet-visible spectroscopic analysis of *Eryngium billardieri* extract, Piperazine, *Eryngium billardieri* bio-synthesized iron nanoparticles & Piperazine encapsulated-*Eryngium billardieri* bio-synthesized iron nanoparticles

Figure 2. Fourier Transform Infrared Spectroscopy analysis of *Eryngium billardieri* extract, Piperazine, *Eryngium billardieri* bio-synthesized iron nanoparticles & Piperazine encapsulated-*Eryngium billardieri* bio-synthesized iron nanoparticles

Figure 3. X-ray Diffraction analysis of (a) *Eryngium billardieri* bio-synthesized iron nanoparticles, (b) Piperazine encapsulated-*Eryngium billardieri* bio-synthesized iron nanoparticles

Figure 4. Field Emission - Scanning Electron Microscopic images of (a) *Eryngium billardieri* bio-synthesized iron nanoparticles, (b) Piperazine encapsulated - *Eryngium billardieri* bio-synthesized iron nanoparticles

Figure 5. X-ray Photoelectron spectrum of Piperazine encapsulated - *Eryngium billardieri* bio-synthesized iron nanoparticles (a) survey scan, (b) XPS spectra of C_{1s}, (c) XPS spectra of N, (d) XPS spectra of O_{1s}, (e) XPS spectra of Fe2p.

Figure 6. Magnetization studies on Piperazine encapsulated - *Eryngium billardieri* bio-synthesized Fe NPs under (a) Zero field cooled mode, (b) field cooled mode, (c) Hysteresis loops, (d) AC susceptibility variations

Figure 7. Energy-dispersive X-ray spectra of (a) *Eryngium billardieri* bio-synthesized iron nanoparticles, (b) Piperazine encapsulated - *Eryngium billardieri* bio-synthesized iron nanoparticles

Figure 8. Photoluminescence spectra of (a) *Eryngium billardieri* bio-synthesized iron nanoparticles, (b) Piperazine encapsulated - *Eryngium billardieri* bio-synthesized iron nanoparticles

Figure 9. BET study indicating Adsorption Desorption of (a) *Eryngium billardieri* bio-synthesized iron nanoparticles, b) Piperazine encapsulated - *Eryngium billardieri* bio-synthesized iron nanoparticles, (c) Pore radius variations of *Eryngium billardieri* bio-synthesized iron nanoparticles, d) Pore radius variations of Piperazine encapsulated - *Eryngium billardieri* bio-synthesized iron nanoparticles,

Figure 10 High-Resolution Transmission Electron Microscopy images of (a) *Eryngium billardieri* bio-synthesized iron nanoparticles and (b) Piperazine encapsulated - *Eryngium billardieri* bio-synthesized iron nanoparticles

Figure 11. Ultraviolet-visible spectroscopic analysis for degradation studies on dye solution using *Eryngium billardieri* bio-synthesized iron nanoparticles & Piperazine encapsulated-*Eryngium billardieri* bio-synthesized iron nanoparticles

Figure 12. Dye degradation using synthesized nanoparticles on (a) Varying the quantity of nanoparticles, (b) Varying initial concentration of aniline yellow dye, (c) Varying the reaction duration, (d) Varying ionic strength of the solution

Figures

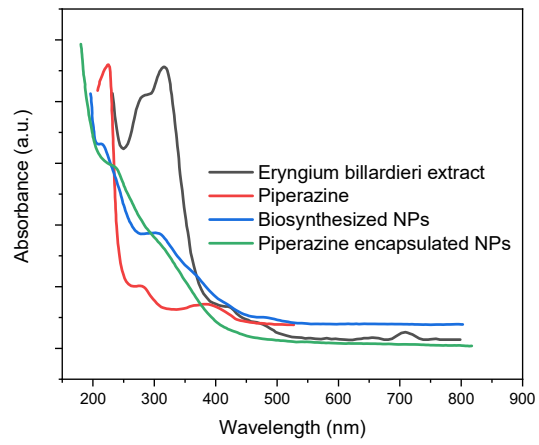


Figure 1

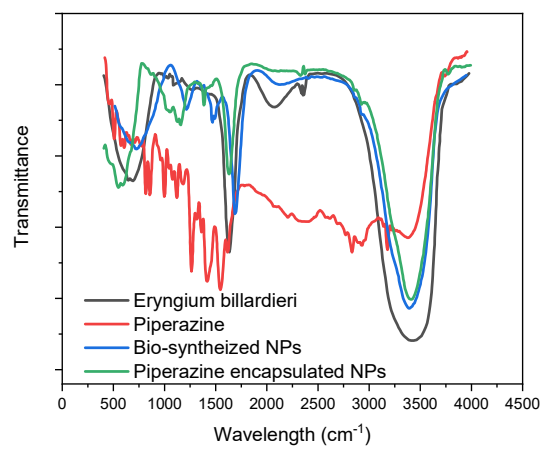
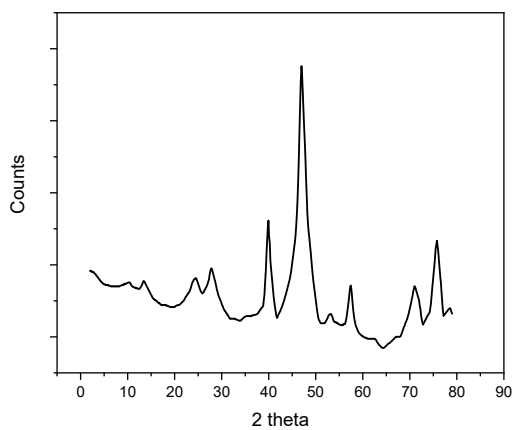
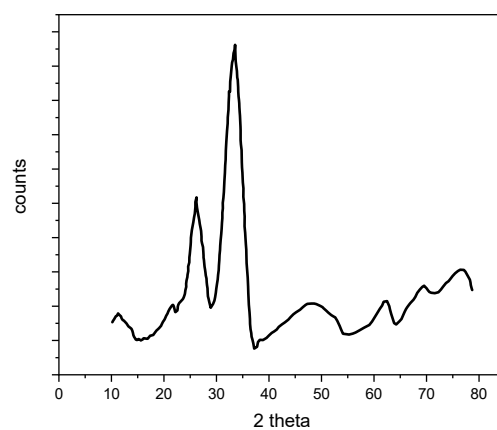


Figure 2

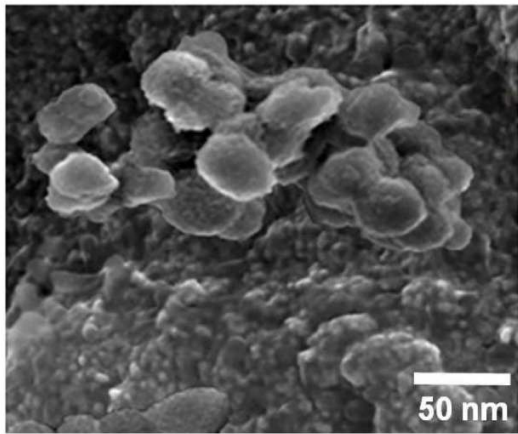


(a)

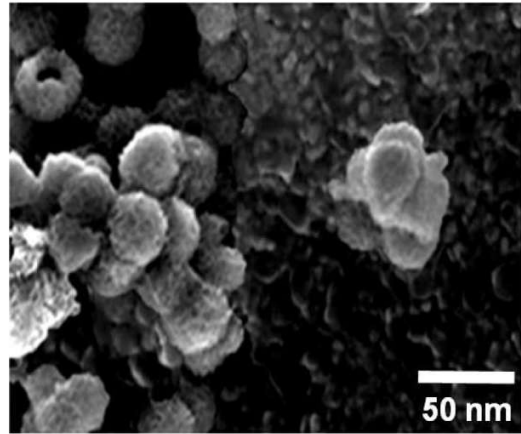


(b)

Figure 3

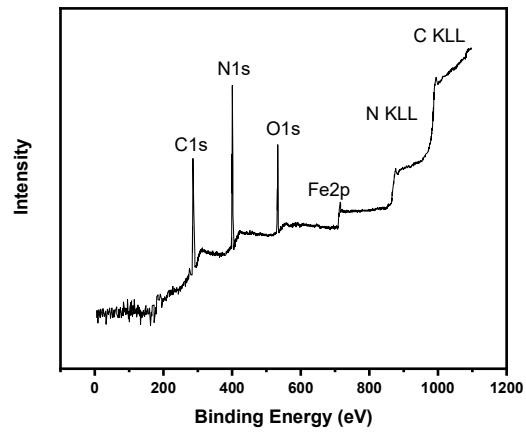


(a)

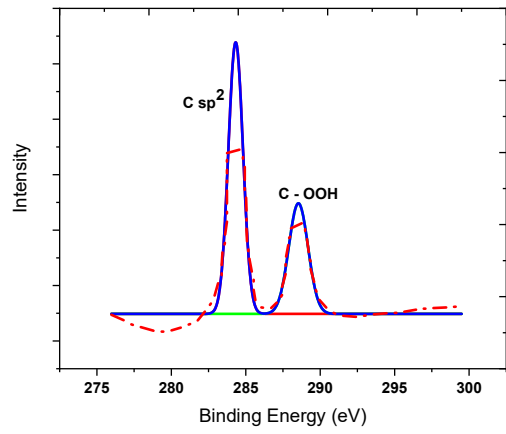


(b)

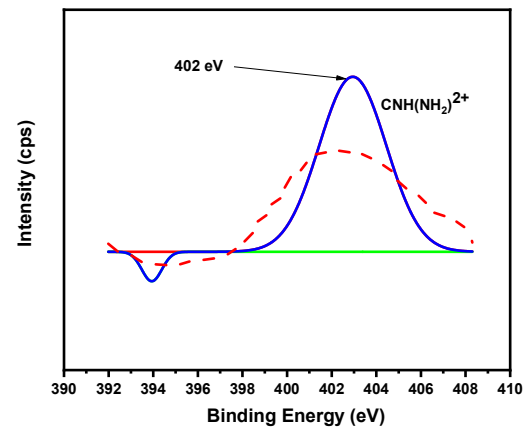
Figure 4



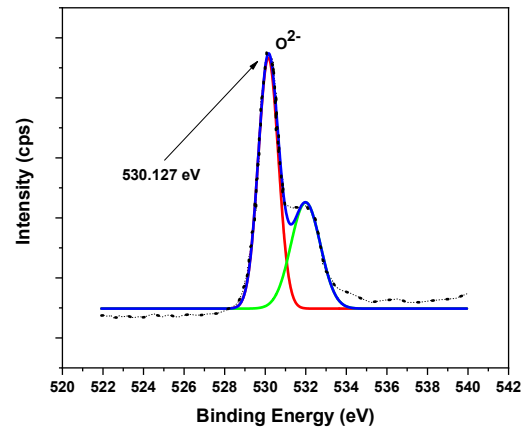
(a)



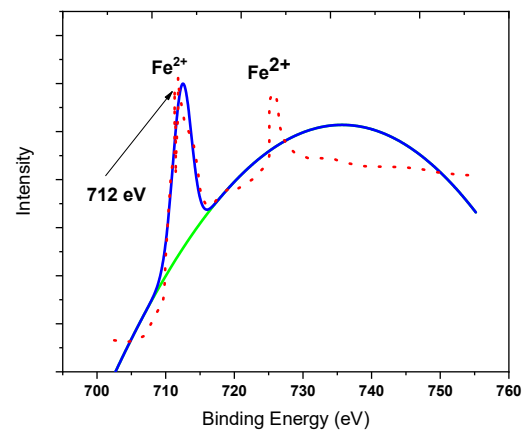
(b)



(c)



(d)



(e)

Figure 5

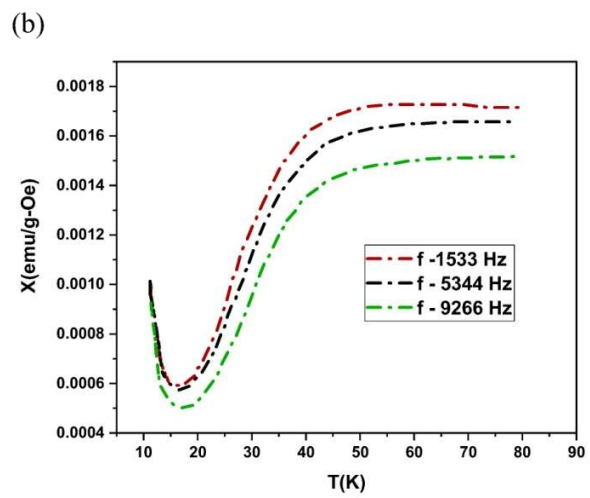
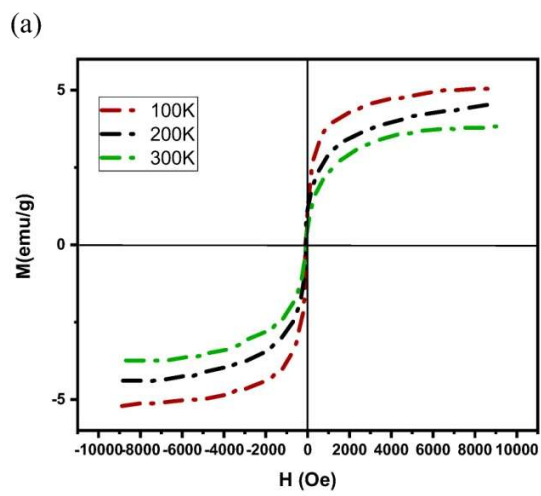
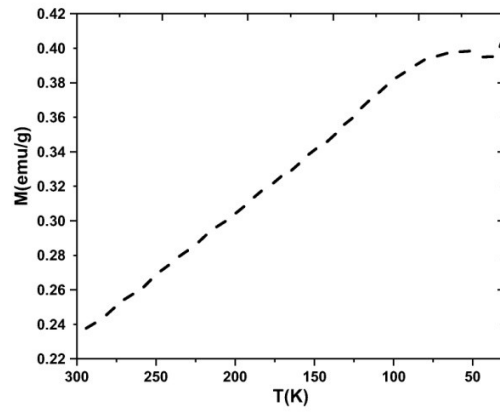
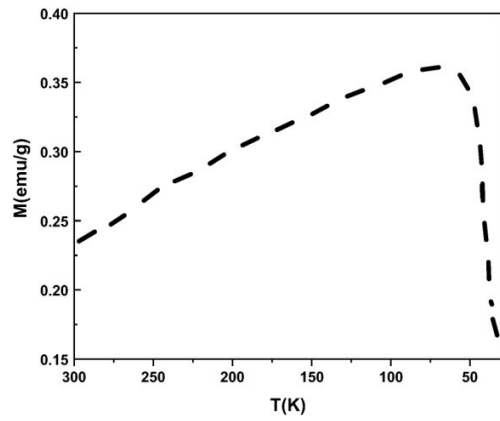
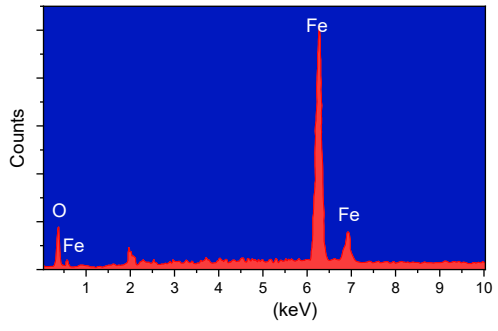
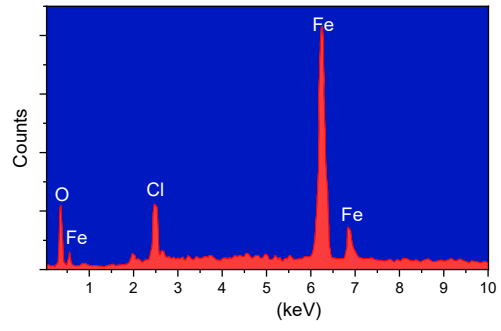


Figure 6



(a)



(b)

Figure 7

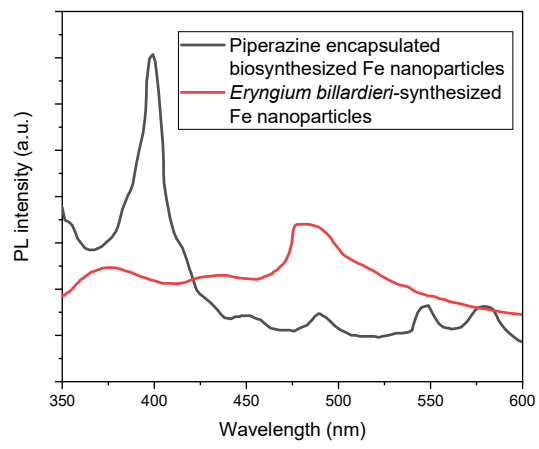
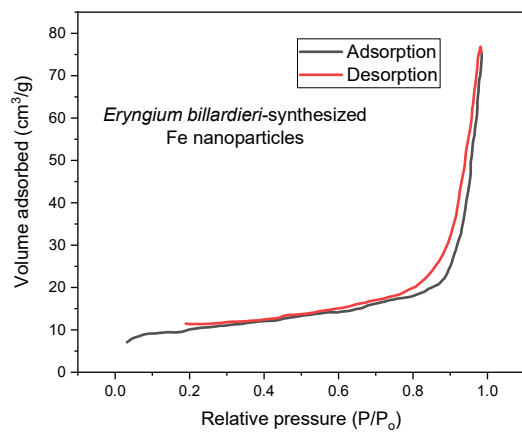
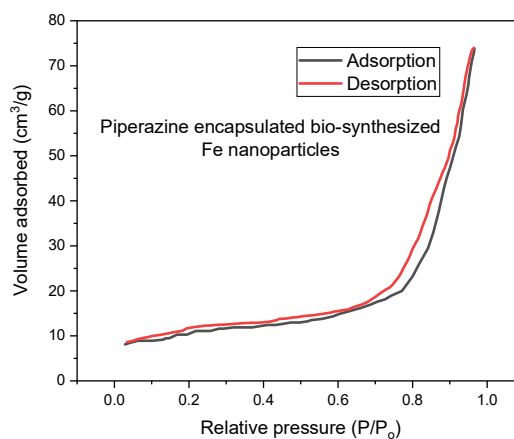


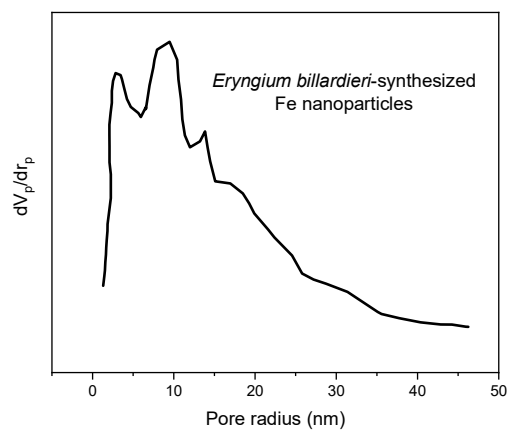
Figure 8



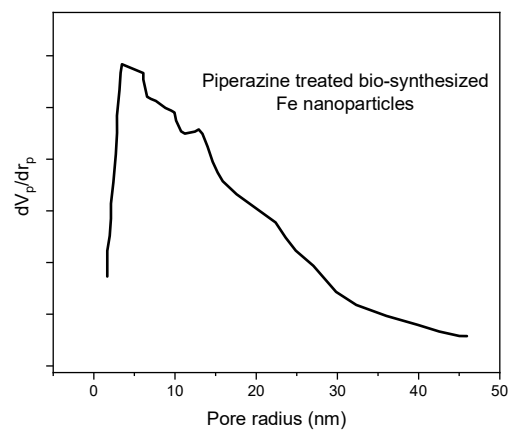
(a)



(b)

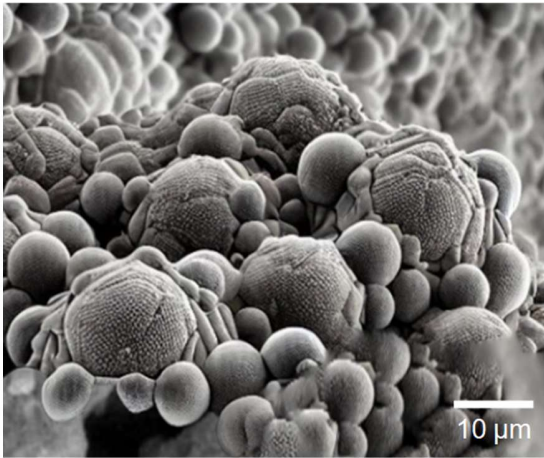


(c)

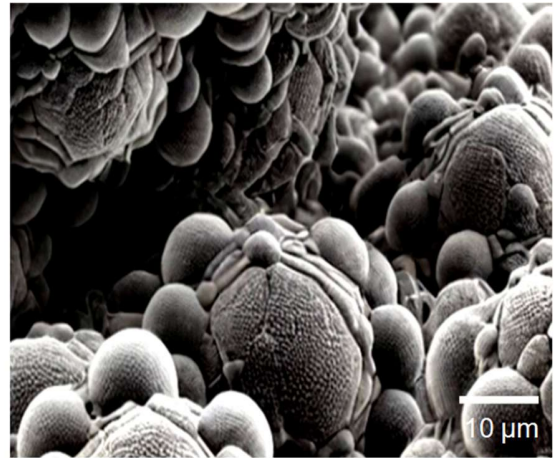


(d)

Figure 9



(a)



(b)

Figure 10

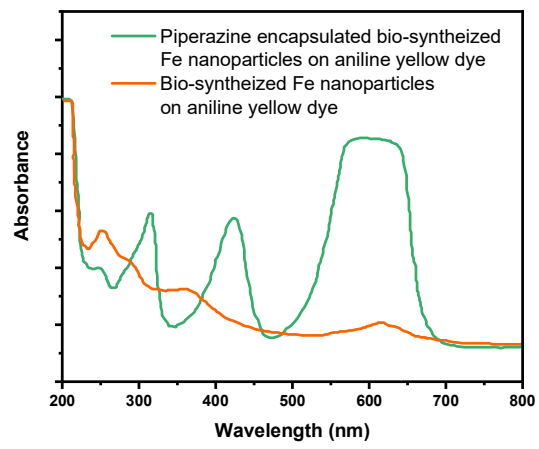


Figure 11

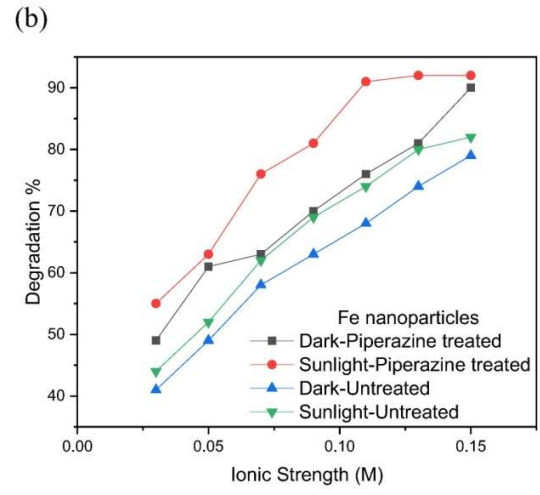
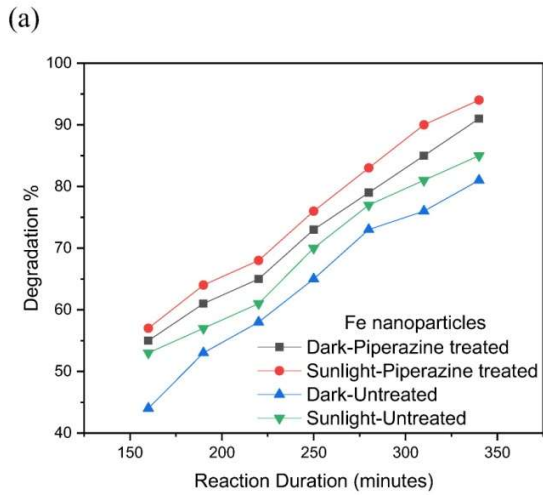
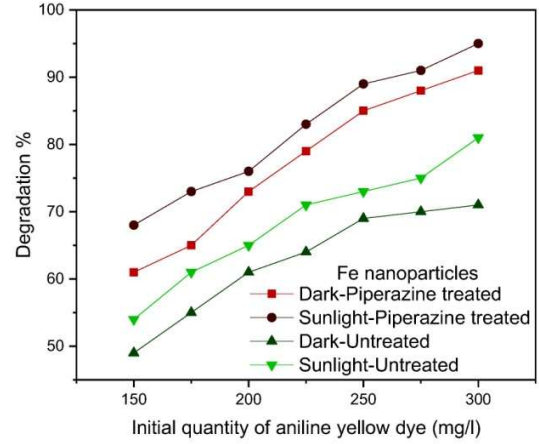
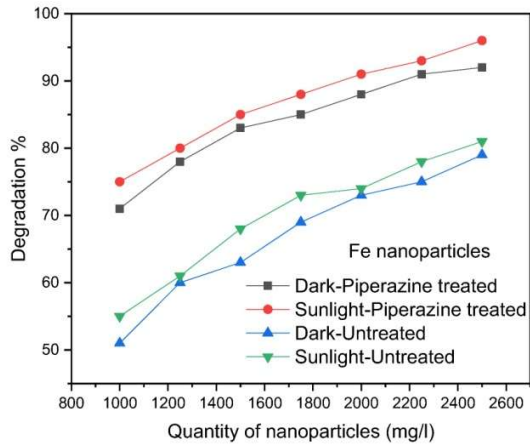


Figure 12